2D MoO3-xSx/MoS2 van der Waals Assembly: a Tunable Heterojunction with Attractive Properties for Photocatalysis

Masoud Shahrokhi, Pascal Raybaud, Tangui Le Bahers

2D $MoO_{3-x}S_x/MoS_2$ van der Waals Assembly: a Tunable Heterojunction with Attractive Properties for Photocatalysis

Masoud Shahrokhi [1], Pascal Raybaud [1,2*] and Tangui Le Bahers [1*]

[1]*Univ Lyon, ENS de Lyon, CNRS, Université Claude Bernard Lyon 1, Laboratoire de Chimie UMR 5182, F-69342 Lyon, France*

[2]*IFP Energies nouvelles, Rond-point de l'échangeur de Solaize, BP 3, 69360 Solaize, France*

Authors for correspondence: pascal.raybaud@ifpen.fr; tangui.le_bahers@ens-lyon.fr

ABSTRACT

2D van der Waals (vdW) heterostructures currently attract much attention in widespread research fields where semiconductors materials are key. With the aim of gaining insights into photocatalytic materials, we use density functional theory (DFT) calculations within HSE06 functional to analyze the evolution of opto-electronic properties and high frequency dielectric constant profiles of various 2D $MoO_{3-x}S_x/MoS_2$ heterostructures modified by chemical and physical approaches. While the MoO_3/MoS_2 heterostructure is a type III heterojunction associated to a metallic character, we find that exchanging with sulfur the terminal-oxo atoms of the $MoO_{3-x}S_x$ single layer (SL) enables to shift its CB position above the VB position of the MoS_2 SL. This trend gives rise to a type II heterojunction where the band gap and charge transfer within the two layers are driven continuously by the S-concentration in $MoO_{3-x}S_x$ SL. This fine tuning leads to a versatile type II heterostructure proposed to provide a direct Z-scheme system valuable for photocatalytic water splitting.

KEYWORDS

MoS_2, MoO_3, heterojunction, Z-scheme, DFT, photocatalysis, water splitting

INTRODUCTION

Two-dimensional (2D) semiconductors heterostructures are widely investigated to design specific electronic devices such as tunneling transistors and light-emitting diodes.[1-3] Another recent exploration of such semiconductors is prompted by the growing interest of photocatalytic materials where the electronic structure of the heterojunction must be tuned to optimize light absorption and separation of the photogenerated charge carriers.[4] Heterojunctions are classified into three types, namely, straddling (type I), staggered (type II), and broken-gap (type III).[5,6] In type I heterojunction and under light irradiation (Figure 1), the electrons and holes accumulate at the conduction band (CB) and the valence band (VB) of SC II, respectively. In type III heterojunction, the CB and the VB levels of SC I have higher potentials than VB of the SC II which breaks the gap. For the type II heterojunction, the CB and VB levels of SC I have higher potentials than the corresponding levels of the SC II. Therefore, thermodynamically, the photogenerated electrons may transfer from SC II to SC I, while the photogenerated holes migrate from SC I to SC II, resulting in a spatial separation of electron-hole pairs. Nevertheless, depending on the relative CB SC I and VB SC II positions and kinetic effects, the photogenerated electrons in SC I may preferentially recombine with the holes from SC II than the transfer of an electron from SC II to SC I. This alternative transfer mode corresponds to a Z-scheme working principle of type II heterojunction,[7,8] where electrons and holes are not only spatially separated but also have a large reductive and oxidative potentials (respectively) making this configuration close to photosynthesis which is appealing for photocatalysis.[7,9,10]

Moreover within such Z-scheme heterojunctions, the maximum photoconversion efficiency in a water-splitting process is theoretically much higher (25%) compared to single semiconductor (12%).[11] This advantage of Z-scheme heterojunction is unfortunately compensated by the

challenges of material synthesis, and of tuning the charge transfer following either a standard type II or a true Z-scheme.[9] One possible way to address these challenges is to explore heterostructures made of the assembly of two-dimensional (2D) layered materials[12] forming stacked 2D/2D layered structures, which electronic properties are weakly affected by the formation of the heterostructure due to the van der Waals (vdW) interaction between layers.

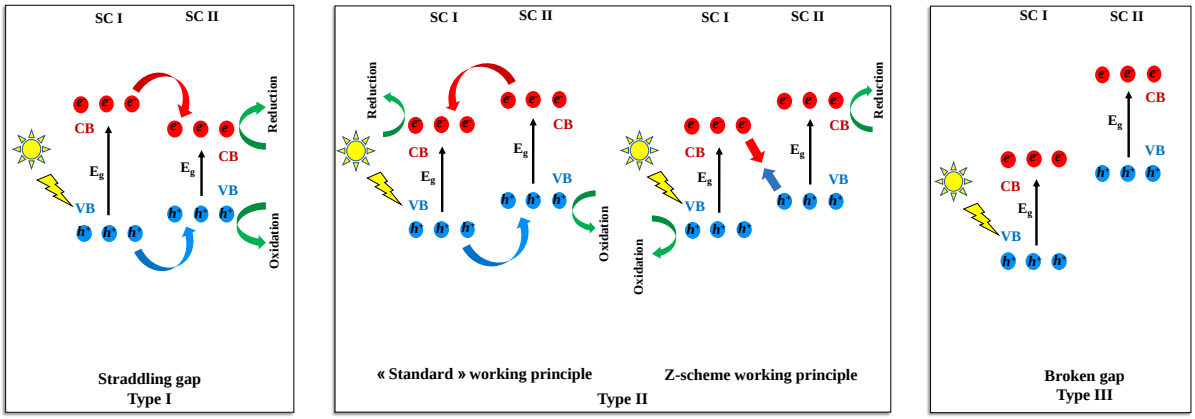

Figure 1. Schematic illustration of the band alignments and charge transfer mechanisms for three different types of heterojunctions formed by coupling of two semiconductors.

Among various 2D nanomaterials, whose graphene is the most well-known representative, 2D transition metal oxides (TMO) and transition metal dichalcogenides (TMD) are actively investigated.[13-17] In particular, α-MoO_3 (*Pnma* space group) is an n-type semiconductor with a wide experimental band gap of ~3.2 eV,[18,19] while 2H-MoS_2 (*P63/mmc* space group) exhibits an indirect band gap of ~1.23 eV.[20,21] Although recent experimental[15,22-26] and theoretical works[25,27,28] highlight the possible synthesis and key interests of MoO_3/MoS_2 heterostructures for various applications, it remains unknown to which extent the optoelectronic properties of such 2D heterostructure can be optimized to match the requirements of photocatalytic materials. DFT with hybrid functional study demonstrated that the MoO_3/MoS_2 heterostructure is a type III

heterojunction, being a good candidate for a tunnel field effect (TFET)-type device[25,28] but not for photocatalytic materials. However, we recently showed by DFT calculations that the optoelectronic properties of α-$MoO_{3-x}S_x$ (S-doped α-MoO_3) and 2H-$MoS_{2-x}O_x$ (O-doped 2H-MoS_2) bulk materials can be tuned by anionic isovalent-atom doping (S and O respectively),[20] which opens opportunities to further explore 2D heterostructures made of α-$MoO_{3-x}S_x$/2H-$MoS_{2-x}O_x$ layers. Hence, the objective of the present work is to explore by DFT (HSE06 functional) how a fine chemical and physical change of the 2D MoO_3/MoS_2 heterostructure can switch the heterojunction from type III to type II heterojunction with adjustable band gaps, relative CB/VB positions, charge transfers and dielectric functions. These new heterostructures are very promising materials for photocatalysis and more generally for semiconductor-based devices.

METHODS

The geometry optimizations of all heterostructures was investigated by means of DFT calculations with periodic boundary condition with the PBE functional[29] as implemented in Vienna ab initio simulation package (VASP)[30,31] and a 3 × 3 × 1 k-point grid. The van der Waals contributions were described by using the semi-empirical Grimme D3 approach[32]. We represented these 2D structures by a periodic array of layers separated by a vacuum region in excess of 20 Å to avoid interactions between periodic images. Electronic wave functions have been expanded using a plane wave basis set with a cutoff energy of 500 eV for the valence electrons. The interaction between the valence and the core electrons for Mo, O and S atoms was described with the projected augmented wave (PAW) method.[33] The convergence criterion for the SCF was set up at 10^{-5} eV/atom. All geometry optimization have been done using the conjugate-gradient method[34] until none of the residual Hellmann−Feynman forces exceeded 10^{-3} eV/Å. Since ordinary DFT within the PBE/GGA

underestimate the band gap, all the electronic properties were computed via single-point calculations by using the range separated hybrid Heyd–Scuseria–Ernzerhof (HSE06) exchange correlation functional[35] on the PBE optimized geometries with a 6 × 6 × 1 k-point mesh using ab initio CRYSTAL17 code.[36] This code works within periodic boundary conditions and adopts localized Gaussian-type function basis sets (BSs) allowing a fast evaluation the Hartree-Fock exchange. The following BSs were used: Mo_SC_HAYWSC-311(d31)G_cora_1997[37] (for Mo atoms), S_86-311G*_lichanot_1993[38] (for S atoms) and O_8-411d11G_valenzano_2006[39] (for O atoms). To calculate the high frequency dielectric function, the electronic density with ($\rho(z)\big|\vec{E}_{ext}$) and without ($\rho(\rho(z)|_0$) external electric field was calculated using CRYSTAL package and averaged in the plane parallel to the *z*-axis. It is then smoothed using a nanoscale averaging[33] along the out-of-plane direction. A more detailed presentation of the procedure is given in SI. The optical properties were calculated through the frequency dependent dielectric matrix $\varepsilon_{\alpha\beta}(\omega)$ within HSE06 functional by using VASP based on a sum overstate approach. The number of empty conduction bands was converged for each structure with respect to standard calculations. The absorption coefficient can be evaluated from dielectric matrix using the Kramers-Kronig transformation:[40]

$$\alpha_{\alpha\beta}(\omega) = \frac{2\omega k_{\alpha\beta}(\omega)}{c} = \frac{\omega \mathrm{Im}(\varepsilon_{\alpha\beta}(\omega))}{c n_{\alpha\beta}(\omega)} \quad (1)$$

where *c* is the speed of light in vacuum. $n_{\alpha\beta}$ and $k_{\alpha\beta}$ are real and imaginary parts of the complex refractive index, and are known as the refractive index and the extinction index, respectively. More details on methods can be found in Supporting Information.

In term of functional, the dielectric-dependent density functional (whose the fraction of Hartree Fock-exchange is inversely proportional to the infinite dielectric constant)[41-43] could be an interesting alternative to the HSE06 functional. However, the difficulty to define the dielectric

constant of a 2D-material and the one of a heterojunction makes the use of such functionals not straightforward. A not-system dependent functional such as HSE06 seems more appropriate for 2D-hterojunction (as illustrated in this work).

RESULTS AND DISCUSSION

Pristine 2D MoO_3/MoS_2 heterostructure. The MoO_3/MoS_2 system was simulated through a (3×3) MoO_3 monolayer supercell with pre-optimized lattice parameters (a = 11.12 Å and b = 11.73 Å) chosen as a substrate of a (4×4) MoS_2 monolayer placed on top of it (Figure 2a). The mismatch of MoS_2 lattice parameters is less than 2% in comparison with the individual layer which ensures a low strain. After optimizing the atomic positions of the heterostructure using DFT-PBE-D3[29,32] functional (see Methods), the equilibrium distance between the O_t-plane of MoO_3 and S-plane of MoS_2, $d_{(S\text{-}Ot)}$ in the MoO_3/MoS_2 heterostructure, is found at 2.86 Å, with an exothermic interlayer binding energy of -0.7 eV.

The band structures and the partial density of states (PDOS) determined with HSE06 functional[35,44] (Figure 2d) show that the MoO_3/MoS_2 interface is a type III heterojunction resulting from the lower CB position of single-layer (SL) MoO_3 (-6.56 eV) than the VB position of SL MoS_2 (-6.36 eV) (Figure 2c), in agreement with the previous theoretical results of Gao et al.[28] A charge transfer occurs from MoS_2 to MoO_3 within the junction (Figure 2b and S3). The differential Bader charge[45] evaluated between the heterojunction and individual layers, reveals a +0.5 charge on MoS_2 layer (-0.5 charge on MoO_3 layer) in the heterostructure. This charge transfer between the layers point to a strong donor–acceptor interaction in MoO_3/MoS_2 composite structure. Since, there is no accumulation of electrons in the interlayer region, the MoO_3 and MoS_2 layers are coupled both by vdW and electrostatic forces.

To overcome the type III heterojunction, CB and VB positions of each distinct MoS_2 and MoO_3 single-layer must be displaced. We first explored a physical approach by increasing the number of layers for each individual component (Supporting Information S2.2 and Figure S2). However, the HSE06 band structure of MoO_3 is relatively insensitive to the number of layers: the band gap varying from 2.83 eV for a monolayer to 2.96 eV for the bulk material. Moreover, the VB and CB edges of MoO_3 nanosheets remain almost unchanged from one monolayer to 5 monolayers. In contrast, the fundamental band gap of MoS_2 layers increases monotonically when the number of layers decreases in good agreement with STM/STS experiments:[46] for single, double and triple layers MoS_2, the calculated bandgaps were 2.38 eV, 1.96 eV and 1.87 eV respectively, while they were measured at 2.40 eV, 2.10 and 1.75 eV respectively (Table S2). It is important to note here that the appropriate bandgap to compare here is the fundamental bandgap and not the optical one (as discussed in the following reference [11]).

More specifically, in MoS_2 nanosheets the CB edge positions remain almost constant while VB edge position shifts to higher energies by increasing the number of layers (Figure S1 and Figure S2). As a consequence, any stacking of MoO_3 and MoS_2 multilayers will not change the type of heterojunction since the relative positions of the MoS_2 multilayers VB and MoO_3 multilayers CB are not inverted, whatever the number of layers considered.

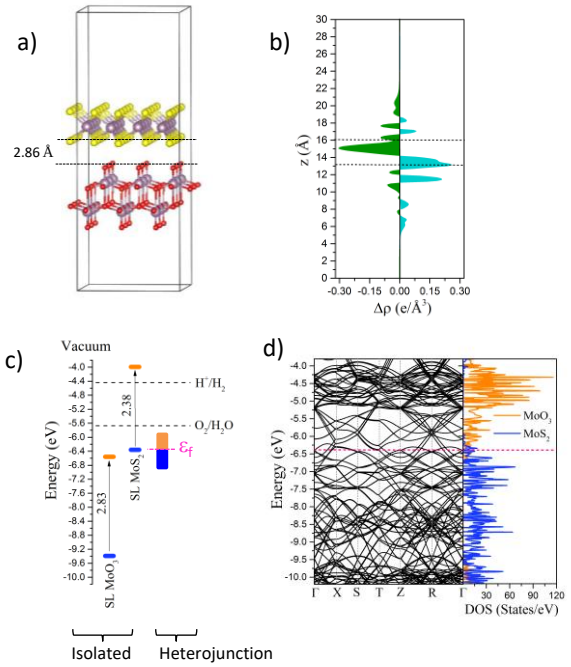

Figure 2. Optimized structure (a), planar-averaged charge density difference ⟨Δρ(z)⟩: electron accumulation in cyan and electron depletion in green (b), conduction and valence band-edge positions respect to vacuum level (c) and band structure and PDOS for each layers (d) for pristine MoO_3/MoS_2 heterojunction. The lower edge of the conduction band (orange colour) and upper edge of the valence band (blue colour) are presented along with the band gap in electron volts. The dashed black lines in (c) indicate the water stability limits for hydrogen and oxygen evolution and the dashed pink lines in (c) and (d) indicate the Fermi energy. The absolute potential of the standard hydrogen electrode was taken as 4.44 eV at a pH = 0**.**

The second approach, more chemical, was inspired by our recent work on doped bulk MoO_3 and MoS_2 materials,[20] and consists in substituting oxygen (sulfur respectively) atoms by sulfur (oxygen respectively) atoms in MoO_3 (MoS_2 respectively) single-layer leading to MoS_xO_{3-x} (MoO_xS_{2-x}) single-layer. The detailed structures, energetic stability and optoelectronic properties of these

systems are reported in the Supporting Information S4. Substituting oxygen atoms (terminal oxo-species preferentially, Figure S4) with sulfur atoms in MoO_3 SL decreases the band gap with values ranging from 2.5 eV to 2.0 eV (Figure 3) while keeping the indirect character of the band gap (Figure S8). This is mainly due to the formation of states located either on S atoms in the band gap or at the top of the VB. The analysis of absolute band edge position indicates that the VB and CB positions of individual SL MoO_3 continuously move to higher energies by increasing S concentration (Figure 3). On the other hand, substituting S atoms with O atoms in MoS_2 SL does not affect neither the band gap nor the CB/VB positions, except for very high concentrations (Figure S9 and S12). In summary, heterostructures combining MoO_3 SL where oxygen is substituted by sulfur atoms with MoS_2 multilayer is the most promising one because it allows a fine tuning of band positions. Assuming first that the bands of each materials will not be affected by the formation of a van der Waals 2D heterojunction, Figure 3 shows that a 2D heterostructure combining a MoS_2 SL with MoO_3 SL doped should enable to switch from a type III to a type II heterojunction by varying the content of S in the $MoO_{3-x}S_x$ SL. In the case of a type II heterojunction, the CB/VB positions seems compatible with water splitting photocatalytic application. It is also important to note that the cell parameters of the S-doped MoO_3 SL are almost not affected by the doping (see Table S3) because only the substitution O_t planes atoms are considered. In other words, the mismatch between S-doped MoO_3 and MoS_2 supercells used to simulate the heterojunction remains low (~2%). The goal of subsequent sections is to investigate whether these proposals based on individual systems remain valid once the heterostructure is explicitly built.

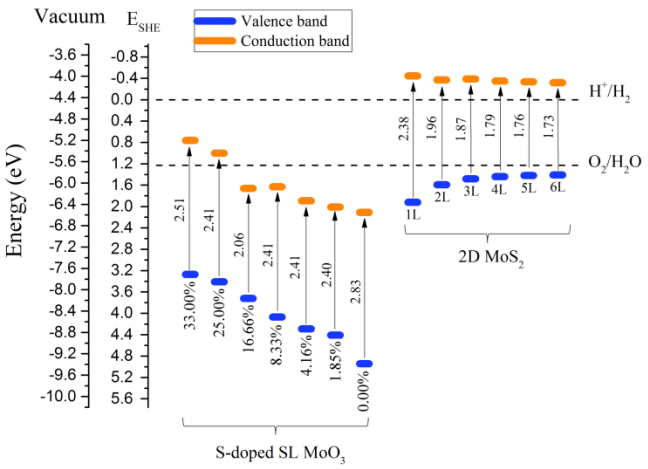

Figure 3. Calculated conduction and valence band-edge positions for S-substituted SL MoO_3 and 1L-6L MoS_2 with respect to vacuum level and standard hydrogen electrode. The lower edge of the conduction band (orange colour) and upper edge of the valence band (blue colour) are presented along with the band gap in electron volts. The dashed black lines indicate the water stability limits for hydrogen and oxygen evolution. The absolute potential of the standard hydrogen electrode was taken as 4.44 eV at a pH = 0.

Type II 2D MoO_3/MoS_2 heterostructure. Figure S13 illustrates the various configurations of MoS_xO_{3-x}/MoS_2 bilayer heterostructures with different concentrations of S atoms replacing the terminal oxo-species of MoO_3. The interlayer distance between MoO_3 and MoS_2 layers is enhanced by increasing the sulfur concentration (Table S5) while interface binding energy becomes more exothermic revealing the enhanced stability of these heterostructures. For low S concentrations into MoO_3 layer (up to 3.75%), the metallic character of the initial MoO_3/MoS_2 heterostructure is maintained while for S concentration equal or greater than 5.6%, a metal-semiconductor transition occurs (Figure S14 and Table S5). As expected from Figure 3 and Figure S14, VB of these materials is located on Mo *4d* states of MoS_2 and the conduction band on the Mo *4d* states of MoO_3 with an indirect band gap. Note that the band gap can only be opened when the doping sulfur atoms are located in the interlayer region. Interestingly, Figure 4 reveals that the

band gap is continuously enlarged by increasing S concentration into MoO_3 layer from 0.15 eV for x_S=5.6% to 1.05 eV for x_S=33% (as suspected from the individual component behaviors, Figure 3). Reversely, the Bader charge transfer decreases with increasing S concentration. For the largest S concentration, it is almost negligible. However, for intermediate S concentration such as 9.3%, this charge transfer is about +0.17 e.

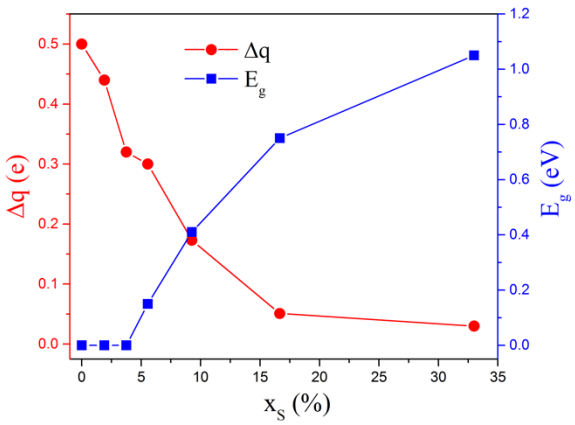

Figure 4. Evolution of the bandgap and the Bader charge transfer of the heterostructure S-doped MoO_3/MoS_2 as a function of the sulfur concentration in MoO_3 layer.

In what follows, we focus on this interesting case of S-doped MoO_3/MoS_2 interface for x_S=9.3% (corresponding to $MoS_{0.28}O_{2.72}$ SL) which exhibits type II character but with a small bandgap (around 0.4 eV). Figure 5 illustrates the optimized structure and electronic properties. The CB position of MoO_3 has higher energy than VB of MoS_2, the Bader charge transfer from MoS_2 to $MoS_{0.28}O_{2.72}$ is decreased (0.17 e^-) with respect to the pristine MoS_2/MoO_3 system (0.5 e^-). This is consistent with the charge density difference plots (Figure 5b and S15), which show electron accumulation in the interlayer region of S-doped MoO_3/MoS_2 indicating a weak covalent bond between the two layers. The PDOS of Figure 5d, shows that the VB and CB of the S-doped MoO_3/MoS_2 interface are delocalized in MoS_2 and $MoS_{0.28}O_{2.72}$ layers respectively, confirming the

formation of the well-defined type II band alignment which facilitates the separation of photo-induced carriers.

The working principle of a type II heterojunction can be "standard", corresponding to the thermodynamic motion of the charge carriers, or a Z-scheme, meaning that kinetically electron and holes will recombine at the interface between the two semiconductors (Figure 1). Tuning properly the bandgap of the type II MoS_xO_{3-x}/MoS_2 heterojunction as a function of S-concentration is probably key to govern the working principle. A large bandgap with a negligible charge transfer (for $x_S \geq 15\%$) favoring the "standard" working principle while a small bandgap (for $x_S \approx$ 9-10%) orienting toward a Z-scheme one. In this latter case, the electron transfer between MoS_2 and MoS_xO_{3-x}, even reduced, is non-negligible which may favor the recombination of electrons and holes at the interface, pushing a little bit more toward a Z-scheme working principle of this heterostructure for photocatalysis. In the case of water splitting, the CB/VB positions of the two semi-conductors with respect to H^+/H and H_2O/O_2 potentials imply that MoS_2 may reduce the proton while $MoS_{0.28}O_{2.72}$ will oxidize water (Figure 5).

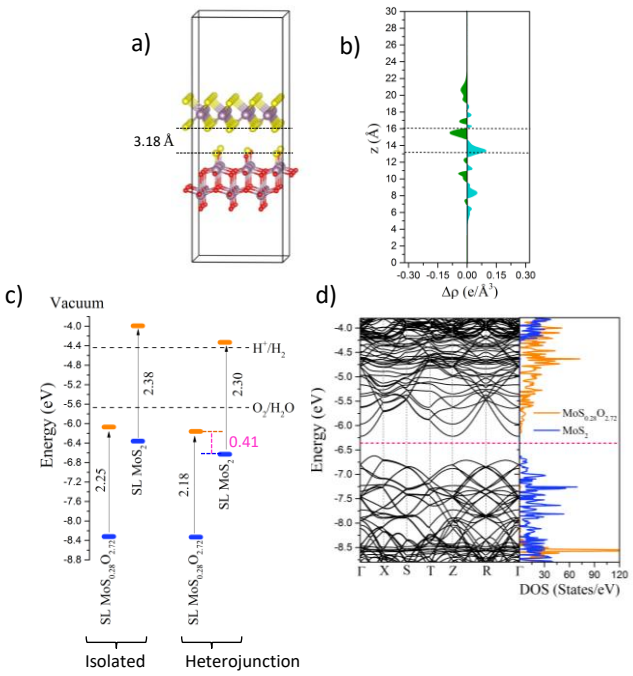

Figure 5. Optimized structure (a), planar-averaged charge density difference ⟨Δρ(z)⟩ (electron accumulation in cyan and electron depletion in green) (b), conduction and valence band-edge positions respect to vacuum level (c) and band structure and PDOS for each layers (d), for S-doped $MoS_{0.28}O_{2.72}/MoS_2$ heterojunction (x_S = 9.3%). The lower edge of the conduction band (orange colour) and upper edge of the valence band (blue colour) are presented along with the band gap in electron volts. The dashed black lines in (c) indicate the water stability limits for hydrogen and oxygen evolution. The absolute potential of the standard hydrogen electrode was taken as 4.44 eV at a pH = 0.

As shown in Supporting Information S4.2, we propose that the S-content of the MoS_xO_{3-x} layer can be reached experimentally by the chemical potential of sulfur imposed by the partial pressure of well-chosen sulfiding agent (such as H_2S or else). It has been reported that Mo-oxysulfide can be synthesized experimentally by sulfiding MoO_3 crystalline compounds or nano-particles dispersed on a support through an O/S exchange process. For instance, the sulfidation of crystalline

MoO_3 by H_2S was characterized by IR and XPS techniques which revealed the possible formation of $MoOS_2$ intermediate.[47] EXAFS experiments revealed the formation of small MoO_xS_y entities from Mo-oxide supported on alumina under H_2/H_2S treatment.[48] Moreover molecular $(NH_4)_2MoO_2S_2$ compounds are known to exist.[49] If so, the transitions from type III to type II heterojunction and within type II from a Z-scheme to a standard working principle could be determined by tuning the given partial pressure of such a sulfiding agent at the preparation step of the material. In photocatalytic reaction conditions, no H_2S is formed which will not modify the properties of the heterojunction. Moreover, the impact of water either as a reactant or as a solvent on the CB/VB positions of the heterojunction should remain minor, since the Mo sites present at the interface exhibit a complete coordination sphere as found in the bulk. So, we suspect that water will mainly interact physically with the heterostructure, while chemical interactions of water will occur on a small number of Mo defect sites located at edges of the 2D-layers of MoO_3 and MoS_2. This interaction of water with the heterostructure should have a minor impact on the opto-electronic properties determined here.

Dielectric profiles of the heterojunctions. While decisive, band positions are not the only important properties of a material for its use as a photocatalyst: the electron-hole separation is also key. To analyze the exciton dissociation, we applied a procedure detailed in Supporting Information 1.3 to evaluate the high frequency dielectric profiles of these new heterostructures.[50-54] It is worth to note in our current work, we employed for the first time, hybrid functional of HSE06[35] to provide accurate estimations. The high frequency dielectric profiles $\varepsilon_\infty(z)$ for individual SL MoO_3, individual SL MoS_2 and S-doped MoO_3/MoS_2 heterojunctions are depicted in Figure 6: a relevant case (MoO_2S) of doping is reported which correspond to the former type II

heterojunctions. Doping S into MoO_3 layer in these heterojunctions obviously enhances the peaks height of dielectric profile of MoO_3 layer but also slightly increases the peaks height of dielectric profile of MoS_2 layer because of the increase of polarity induced by sulfur. As a consequence, the effective dielectric constants, ε_{eff}, of the S-doped MoO_3 heterojunctions is greater (4.49) than the one of MoO_3 (2.85). Moreover, the effective dielectric constant of the S-doped MoO_3/MoS_2 interface is also slightly larger (4.52) than the sum of the individual SL MoO_3 and SL MoS_2 (4.33) when considered as non-interacting probably because of the covalent interaction between the two layers increasing the polarizability of the interface.

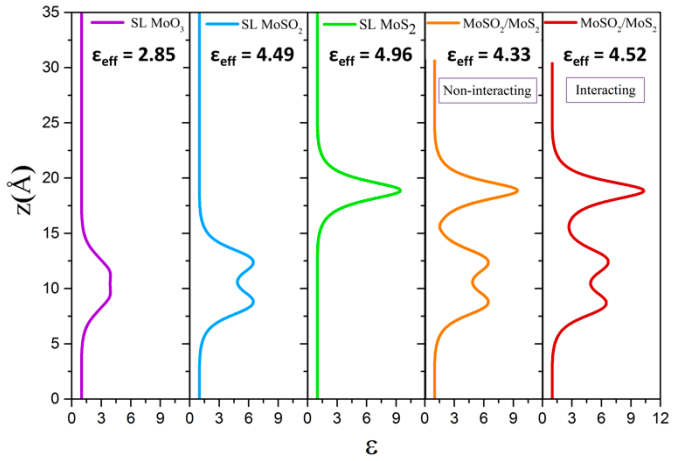

Figure 6. The high frequency dielectric constant profile along out-of-plane for SL MoO_3, $MoSO_2$, MoS_2 and $MoSO_2/MoS_2$ hetero-structures. The effective dielectric constant for each structure is also reported in the caption.

The optical analysis for S-doped MoO_3/MoS_2 heterojunctions (Figure S17) indicates highly anisotropic optical properties for all 2D systems along in-plane and out-of-plane. The absorption coefficient of S-doped MoO_3/MoS_2 heterojunctions is higher than SL MoO_3 in the UV-vis window and it enhances by increasing S concentration in the structures. In general, despite the indirect band gap nature of these heterojunctions, high absorption coefficients were attained (~10^5 cm^{-1}) that is

higher than the typical absorption coefficient value for direct band gap semiconductors across the entire UV-vis range[20]. These two complementary properties confirm the high potential interest of S-doped MoO_3/MoS_2 heterojunctions.

Sensitivity to the number of layers involved in the heterostructure. In order to optimize at best the composite material, we also investigate the impact of varying the number of MoS_2 and MoO_2S layers in the heterostructures. Although we have already shown that the number of layers was not impacting the individual component of the heterostructure, it remains key to determine how the MoS_2/MoO_2S heterojunction itself depends on the number of layers. This analysis could provide practical insights into the further design of the materials regarding its sensitivity to layers' stacking during the synthesis step.

Thus, we explore the impact of increasing the MoS_2 and MoO_3 layers on the optoelectronic properties and as well as the VB and CB band positions of their formed interface. We first consider the case of two MoS_2 layers (2L) in the S-doped MoO_3 (x_S=33%)/MoS_2 heterostructure. The interlayer binding energy for S-doped MoO_3/2L-MoS_2 interface is -1.2 eV indicating a stabilizing effect for this composite by increasing the number of layers. Figure 7a and b illustrates the optimized structure and the VB and CB band positions of S-doped MoO_3/2L-MoS_2 heterostructure. This heterostructure shows a band gap of 1.02 eV allowing us to conclude that the increasing the number of MoS_2 layer has a weak effect on S-doped MoO_3/MoS_2 heterostructure in terms of band gap. Regarding to their CB and VB band positions, this interface forms a type II heterostructure. Figure S19 shows that the electrons are accumulated in the interlayer regions of S-doped MoO_3/MoS_2 and of MoS_2/MoS_2 indicating the weak covalent bond between these layers. The Bader charge analysis indicates that a weak electron transfer (0.025 e^-) from MoS_2 layer at middle

to $MoSO_2$ layer while the topmost MoS_2 layer keeps its charge unchanged. From this point of view, the increase of the number of layers does not impact tremendously the heterojunction. Figure S20 presents the dielectric constant profile for S-doped MoO_3/2L-MoS_2 heterostructure. Our results show that the peaks of dielectric profile in $MoSO_2$/2L-MoS_2 interface are significantly enhanced. The reason for this increase is the interaction between S atoms at the nearest layers.

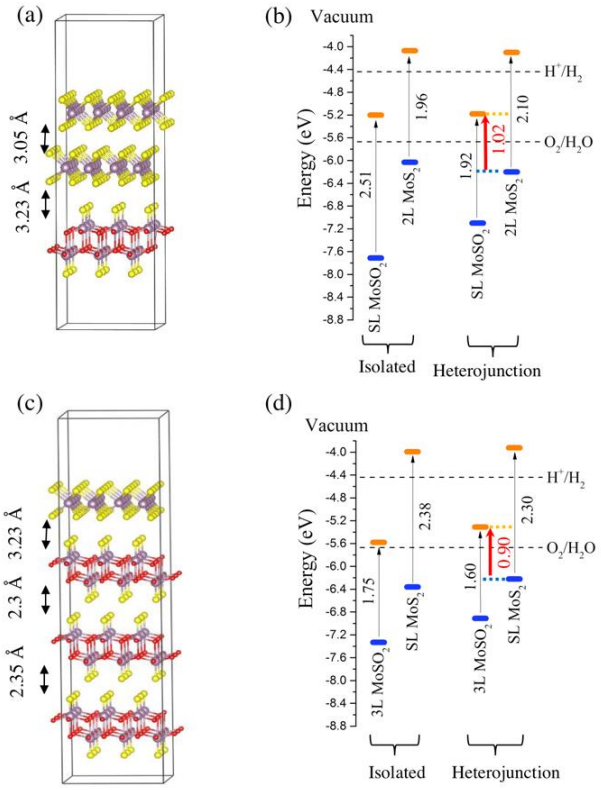

Figure 7. Optimized structure and conduction and valence band-edge positions respect to vacuum level for S-doped MoO_3/2L-MoS_2 (a)-(b) and 3L-S-doped-MoO_3/MoS_2 (c)-(d) heterostructures. The lower edge of the conduction band (orange colour) and upper edge of the valence band (blue colour) are presented along with the band gap in electron volts. The dashed black lines indicate the water stability limits for hydrogen and oxygen evolution. The absolute potential of the standard hydrogen electrode was taken as 4.44 eV at a pH = 0.

In a second step, we now consider a heterostructure with 3 MoO_3 layers. As discussed before, increasing the number of pristine MoO_3 layers does not produce any change in the VB and CB positions on this material alone. Nevertheless, doping S into MoO_3 can shift the VB and CB positions depending on sulfur concentration. Hence, two different systems of S-doped 3L-MoO_3/MoS_2 interface with low and high sulfur concentrations were studied: (i) 3L-$MoS_{0.17}O_{2.83}$/MoS_2 where only the top layer (interfacial) of O-atoms are substituted by S and (ii) 3L-$MoSO_2$/MoS_2. Figure S21 shows that 3L-$MoS_{0.17}O_{2.83}$/MoS_2 has almost a metallic character (bandgap computed around 0.02 eV), although this metallic character is less pronounced than in the former MoO_3/MoS_2 case. The 3L-$MoSO_2$/MoS_2 is a type II heterostructure with a band gap of 0.9 eV (Figure 7c and d) with a similar feature as 1L-S-doped-MoO_3/MoS_2. Since the band gap is decreased by 0.1 eV with respect to the 1L-S-doped-MoO_3/MoS_2 we suspect that this is probably a more favorable configuration for building a Z-scheme system. Furthermore, the effective dielectric function was estimated to be 5.65 and 5.40 for $MoSO_2$/2L-MoS_2 and 3L-$MoSO_2$/MoS_2 interfaces which are greater than that for 1L-$MoSO_2$/MoS_2 system (4.52).

To go beyond the type II-band alignment, it is important to mention that the proposed heterostructure is also a good candidate for photocatalytic applications since it may potentially generate a direct Z-scheme system. Within such as a Z-scheme, the photogenerated electron in the CB of S-doped-MoO_3 will recombine to the photogenerated hole in the VB of MoS_2 leading to very reductant electrons in MoS_2 and oxidant holes in S-doped MoO_3. This 2 photons process can potentially lead to efficient photoelectrochemical reaction, including water splitting. It is beyond the scope of the present work to determine if such a Z-scheme may preferentially occur to the type-II heterojunction, because this depends on numerous intricate complex effects such as the internal

electric field, band bending, and dynamics of charge carrier. However, we think that this heterostructure deserves to be investigated since it appears that its bandgap, probably one of the main parameters orienting toward type-II or Z-scheme working principle, can be tuned by adapting the number of layers of MoS_2 and the S-doping level in MoO_3.

CONCLUSIONS

Through DFT calculations, we proposed strategies to tune the transitions from type III to type II band alignment of materials made of 2D $MoO_{3-x}S_x/MoS_2$ heterostructure. We found that the optoelectronic properties, absolute valence and conduction band edge positions and high frequency dielectric constant profile of individual 2D MoO_3 and MoS_2 components can be effectively modulated by S-substitution of terminal-oxo species inside the $MoO_{3-x}S_x$ structure. This class of material may thus exhibit a large number of applications depending on the targeted type of heterojunction obtained at low/medium/high S-doping.

At zero or low S-doping (≤5%), the heterostructure exhibits a type III heterojunction, while for high S-doping (≥15%), the band gap may encompass 1 eV. Interesting, at medium and high S-doping (>5%), the band-gap and charge transfer of the $MoS_2/MoO_{3-x}S_x$ heterostructure evolves continuously with the S-concentration in the $MoO_{3-x}S_x$. In particular, at medium S-doping (9-10%), we identified a 2D $MoS_{0.28}O_{2.72}/MoS_2$ heterostructure as a potential photocatalytic material since it may potentially generate a direct Z-scheme system due to the proximity of the CB of S-doped-MoO_3 to the VB of MoS_2 (band gap ~ 0.4 eV). Within such as a Z-scheme, the photogenerated electron in the CB of S-doped-MoO_3 will recombine to the photogenerated hole in the VB of MoS_2 leading to reducing electrons in MoS_2 and oxidant holes in S-doped MoO_3. We also show that our finding can be extended to heterojunctions with variable numbers of layers

MoS_2 and $MoO_{3-x}S_x$ which certainly offers more versality to the experimental synthesis of these nano-materials. Moreover, according to our thermodynamic analysis, such MoS_xO_{3-x} structures should be accessible experimentally by well-defined sulfiding agents and conditions which will allow the selective S-substitution of terminal-oxo species present in the MoO_3 layer.

One perspective of the present work could be to determine for which S-doping such a Z-scheme may occur preferentially to the type II heterojunction, by considering intricate effects such as the internal electric field, band bending, and kinetics of charge carriers. Hopefully, this work will open new route for exploring semiconductors made of 2D-heterojunctions with flexible type III/type II transition.

ASSOCIATED CONTENT

Supporting Information

The supporting information contains the details of the thermodynamic analysis; the details of absolute valence and conduction band edge positions; the details of the optoelectronic properties; the details of high frequency dielectric constant of O-doped 2D MoS_2 and S-doped 2D MoO_3 nanosheets. It also contains the structural and electronic properties of S-doped MoO_3/MoS_2 interface with different S concentration and configuration; the dielectric constant profile for S-doped MoO_3/2L-MoS_2, and S-doped 3L-$MoSO_2/MoS_2$ interfaces. The details of the methodology and computational setup alongside with the method to obtain the microscopic dielectric constant profile for 2D materials is also presented in supporting information. Finally, the most relevant structures, in POSCAR format, are also reported in Supporting Information

AUTHOR INFORMATION

Corresponding Authors

*E-mail: tangui.le_bahers@ens-lyon.fr

ORCID: Tangui Le Bahers: 0000-0003-2166-081X

*E-mail: pascal.raybaud@ifpen.fr

ORCID: Pascal Raybaud: 0000-0003-4506-5062

ACKNOWLEDGMENTS

This work is part of the "RatiOnAl Design for CATalysis" (ROAD4CAT) industrial chair, project IDEXLYON funded by the French National Research Agency (ANR-16-IDEX-0005) and the Commissariat-General for Investment (CGI) within the framework of Investissements d'Avenir program ("Investment for the future"). The authors thank the SYSPROD project and AXELERA Pôle de Compétitivité for financial support (PSMN Data Center). This work was granted access to the HPC resources of CINES, IDRIS and TGCC under the allocation 2018-080609 made by GENCI.

References

(1) Wang, X.; Xia, F.: Stacked 2d Materials Shed Light. *Nat. Mater.* **2015**, *14*, 264-265.

(2) Withers, F.; Del Pozo-Zamudio, O.; Mishchenko, A.; Rooney, A. P.; Gholinia, A.; Watanabe, K.; Taniguchi, T.; Haigh, S. J.; Geim, A. K.; Tartakovskii, A. I.; Novoselov, K. S.:

Light-Emitting Diodes by Band-Structure Engineering in Van Der Waals Heterostructures. *Nat. Mater.* **2015**, *14*, 301-306.

(3) Novoselov, K. S.; Mishchenko, A.; Carvalho, A.; Neto, A. H. C.: 2d Materials and Van Der Waals Heterostructures. *Science* **2016**, *353*, 6298.

(4) Kou, J.; Lu, C.; Wang, J.; Chen, Y.; Xu, Z.; Varma, R. S.: Selectivity Enhancement in Heterogeneous Photocatalytic Transformations. *Chem. Rev.* **2017**, *117*, 1445-1514.

(5) Özçelik, V. O.; Azadani, J. G.; Yang, C.; Koester, S. J.; Low, T.: Band Alignment of Two-Dimensional Semiconductors for Designing Heterostructures with Momentum Space Matching. *Phys. Rev. B* **2016**, *94*, 035125.

(6) Lei, C.; Ma, Y.; Xu, X.; Zhang, T.; Huang, B.; Dai, Y.: Broken-Gap Type-Iii Band Alignment in WTe_2/HfS_2 Van Der Waals Heterostructure. *J. Phys. Chem. C* **2019**, *123*, 23089-23095.

(7) Wang, Y.; Suzuki, H.; Xie, J.; Tomita, O.; Martin, D. J.; Higashi, M.; Kong, D.; Abe, R.; Tang, J.: Mimicking Natural Photosynthesis: Solar to Renewable H_2 Fuel Synthesis by Z-Scheme Water Splitting Systems. *Chem. Rev.* **2018**, *118*, 5201-5241.

(8) Maeda, K.: Z-Scheme Water Splitting Using Two Different Semiconductor Photocatalysts. *ACS Catal.* **2013**, *3*, 1486-1503.

(9) Xu, Q.; Zhang, L.; Yu, J.; Wageh, S.; Al-Ghamdi, A. A.; Jaroniec, M.: Direct Z-Scheme Photocatalysts: Principles, Synthesis, and Applications. *Mater. Today* **2018**, *21*, 1042-1063.

(10) Xia, X.; Song, M.; Wang, H.; Zhang, X.; Sui, N.; Zhang, Q.; Colvin, V. L.; Yu, W. W.: Latest Progress in Constructing Solid-State Z Scheme Photocatalysts for Water Splitting. *Nanoscale* **2019**, *11*, 11071-11082.

(11) Le Bahers, T.; Takanabe, K.: Combined Theoretical and Experimental Characterizations of Semiconductors for Photoelectrocatalytic Applications. *J. Photochem. Photobiol. C: Photochem. Rev.* **2019**, *40*, 212-233.

(12) Su, J.; Li, G.-D.; Li, X.-H.; Chen, J.-S.: 2d/2d Heterojunctions for Catalysis. *Adv. Sci.* **2019**, *6*, 1801702.

(13) Yang, T.; Song, T. T.; Callsen, M.; Zhou, J.; Chai, J. W.; Feng, Y. P.; Wang, S. J.; Yang, M.: Atomically Thin 2d Transition Metal Oxides: Structural Reconstruction, Interaction with Substrates, and Potential Applications. *Adv. Mater. Interfaces* **2019**, *6*, 1801160.

(14) Mak, K. F.; Lee, C.; Hone, J.; Shan, J.; Heinz, T. F.: Atomically Thin MoS_2: A New Direct-Gap Semiconductor. *Phys. Rev. Lett.* **2010**, *105*, 136805.

(15) Kumar, R.; Goel, N.; Mishra, M.; Gupta, G.; Fanetti, M.; Valant, M.; Kumar, M.: Growth of MoS_2–MoO_3 Hybrid Microflowers Via Controlled Vapor Transport Process for Efficient Gas Sensing at Room Temperature. *Adv. Mater. Interfaces* **2018**, *5*, 1800071.

(16) Sun, J.; Li, X.; Guo, W.; Zhao, M.; Fan, X.; Dong, Y.; Xu, C.; Deng, J.; Fu, Y.: Synthesis Methods of Two-Dimensional MoS_2: A Brief Review. *Crystals* **2017**, *7*, 198.

(17) Cai, L.; McClellan, C. J.; Koh, A. L.; Li, H.; Yalon, E.; Pop, E.; Zheng, X.: Rapid Flame Synthesis of Atomically Thin MoO_3 Down to Monolayer Thickness for Effective Hole Doping of WSe_2. *Nano Lett.* **2017**, *17*, 3854-3861.

(18) Carcia, P. F.; McCarron, E. M.: Synthesis and Properties of Thin Film Polymorphs of Molybdenum Trioxide. *Thin Solid Films* **1987**, *155*, 53-63.

(19) Chu, C.-W.; Li, S.-H.; Chen, C.-W.; Shrotriya, V.; Yang, Y.: High-Performance Organic Thin-Film Transistors with Metal Oxide/Metal Bilayer Electrode. *Appl. Phys. Lett.* **2005**, *87*, 193508.

(20) Shahrokhi, M.; Raybaud, P.; Bahers, T. L.: On the Understanding of the Optoelectronic Properties of S-Doped MoO_3 and O-Doped MoS_2 Bulk Systems: A DFT Perspective. *J. Mater. Chem. C* **2020,** *8*, 9064-9074.

(21) Kam, K. K.; Parkinson, B. A.: Detailed Photocurrent Spectroscopy of the Semiconducting Group Vib Transition Metal Dichalcogenides. *J. Phys. Chem.* **1982**, *86*, 463-467.

(22) Yoon, A.; Kim, J. H.; Yoon, J.; Lee, Y.; Lee, Z.: Van Der Waals Epitaxial Formation of Atomic Layered a-MoO_3 on MoS_2 by Oxidation. *ACS Appl. Mater. Interfaces* **2020**, *12*, 22029-22036.

(23) Yin, Z.; Zhang, X.; Cai, Y.; Chen, J.; Wong, J. I.; Tay, Y.-Y.; Chai, J.; Wu, J.; Zeng, Z.; Zheng, B.; Yang, H. Y.; Zhang, H.: Preparation of MoS_2–MoO_3 Hybrid Nanomaterials for Light-Emitting Diodes. *Angew. Chem. Int. Ed.* **2014**, *53*, 12560-12565.

(24) Chen, Z.; Cummins, D.; Reinecke, B. N.; Clark, E.; Sunkara, M. K.; Jaramillo, T. F.: Core–Shell MoO_3–MoS_2 Nanowires for Hydrogen Evolution: A Functional Design for Electrocatalytic Materials. *Nano Lett.* **2011**, *11*, 4168-4175.

(25) C, S. K.; Longo, R. C.; Addou, R.; Wallace, R. M.; Cho, K.: Electronic Properties of MoS_2/MoO_x Interfaces: Implications in Tunnel Field Effect Transistors and Hole Contacts. *Sci. Rep.* **2016**, *6*, 33562.

(26) Tessarek, C.; Gridenco, O.; Wiesing, M.; Müssener, J.; Figge, S.; Sebald, K.; Gutowski, J.; Eickhoff, M.: Controlled Laser-Thinning of MoS_2 Nanolayers and Transformation to Amorphous MoO_x for 2d Monolayer Fabrication. *ACS Applied Nano Mater.* **2020**, *3*, 7490-7498.

(27) Li, H.; Yu, K.; Tang, Z.; Fu, H.; Zhu, Z.: High Photocatalytic Performance of a Type-Ii A-MoO_3@MoS_2 Heterojunction: From Theory to Experiment. *Phys. Chem. Chem. Phys.* **2016**, *18*, 14074-14085.

(28) Gao, Z.; Zhou, Z.; Tománek, D.: Degenerately Doped Transition Metal Dichalcogenides as Ohmic Homojunction Contacts to Transition Metal Dichalcogenide Semiconductors. *ACS Nano* **2019**, *13*, 5103-5111.

(29) Perdew, J. P.; Burke, K.; Ernzerhof, M.: Generalized Gradient Approximation Made Simple. *Phys. Rev. Lett.* **1996**, *77*, 3865-3868.

(30) Kresse, G.; Furthmüller, J.: Efficient Iterative Schemes for Ab Initio Total-Energy Calculations Using a Plane-Wave Basis Set. *Phys. Rev. B* **1996**, *54*, 11169-11186.

(31) Kresse, G.; Furthmüller, J.: Efficiency of Ab-Initio Total Energy Calculations for Metals and Semiconductors Using a Plane-Wave Basis Set. *Comput. Mater. Sci.* **1996**, *6*, 15-50.

(32) Grimme, S.; Antony, J.; Ehrlich, S.; Krieg, H.: A Consistent and Accurate Ab Initio Parametrization of Density Functional Dispersion Correction (Dft-D) for the 94 Elements H-Pu. *J. Chem. Phys.* **2010**, *132*, 154104.

(33) Blöchl, P. E.: Projector Augmented-Wave Method. *Phys. Rev. B* **1994**, *50*, 17953-17979.

(34) Hestenes, M. R.; Stiefel, E.: Methods of Conjugate Gradients for Solving Linear Systems. *J. Res. Natl. Bureau Standards* **1952**, *49*, 409-436.

(35) Krukau, A. V.; Vydrov, O. A.; Izmaylov, A. F.; Scuseria, G. E.: Influence of the Exchange Screening Parameter on the Performance of Screened Hybrid Functionals. *J. Chem. Phys.* **2006**, *125*, 224106.

(36) Dovesi, R.; Erba, A.; Orlando, R.; Zicovich-Wilson, C. M.; Civalleri, B.; Maschio, L.; Rérat, M.; Casassa, S.; Baima, J.; Salustro, S.; Kirtman, B.: Quantum-Mechanical Condensed Matter Simulations with Crystal. *WIREs Comput. Mol. Sci.* **2018**, *8*, e1360.

(37) Corà, F.; Patel, A.; Harrison, N. M.; Roetti, C.; Richard A. Catlow, C.: Anab Initio Hartree–Fock Study of a-MoO_3. *J. Mater. Chem.* **1997**, *7*, 959-967.

(38) Lichanot, A.; Aprà, E.; Dovesi, R.: Quantum Mechnical Hartree-Fock Study of the Elastic Properties of Li_2S and Na_2S. *Physica Status Solidi (b)* **1993**, *177*, 157-163.

(39) Valenzano, L.; Torres, F. J.; Doll, K.; Pascale, F.; Zicovich-Wilson, C. M.; Dovesi, R.: Ab Initio Study of the Vibrational Spectrum and Related Properties of Crystalline Compounds; the Case of $CaCo_3$ Calcite. *Z. Phys. Chem.* **2006**, *220*, 893-912.

(40) Wooten, F.: *Optical Properties of Solids*; Academic Press, 2013.

(41) Conesa, J. C.: Band Structures and Nitrogen Doping Effects in Zinc Titanate Photocatalysts. *Catal. Today* **2013**, *208*, 11-18.

(42) Das, T.; Di Liberto, G.; Tosoni, S.; Pacchioni, G.: Band Gap of 3d Metal Oxides and Quasi-2d Materials from Hybrid Density Functional Theory: Are Dielectric-Dependent Functionals Superior? *J. Chem. Theory Comput.* **2019**, *15*, 6294-6312.

(43) Brawand, N. P.; Vörös, M.; Govoni, M.; Galli, G.: Generalization of Dielectric-Dependent Hybrid Functionals to Finite Systems. *Phys. Rev. X* **2016**, *6*, 041002.

(44) Heyd, J.; Scuseria, G. E.; Ernzerhof, M.: Hybrid Functionals Based on a Screened Coulomb Potential. *J. Chem. Phys.* **2003**, *118*, 8207-8215.

(45) Henkelman, G.; Arnaldsson, A.; Jónsson, H.: A Fast and Robust Algorithm for Bader Decomposition of Charge Density. *Comput. Mater. Sci.* **2006**, *36*, 354-360.

(46) Huang, Y. L.; Chen, Y.; Zhang, W.; Quek, S. Y.; Chen, C.-H.; Li, L.-J.; Hsu, W.-T.; Chang, W.-H.; Zheng, Y. J.; Chen, W.; Wee, A. T. S.: Bandgap Tunability at Single-Layer Molybdenum Disulphide Grain Boundaries. *Nat. Commun.* **2015**, *6*, 6298.

(47) Weber, T.; Muijsers, J. C.; van Wolput, J. H. M. C.; Verhagen, C. P. J.; Niemantsverdriet, J. W.: Basic Reaction Steps in the Sulfidation of Crystalline MoO_3 to MoS_2, as Studied by X-Ray Photoelectron and Infrared Emission Spectroscopy. *J. Phys. Chem.* **1996**, *100*, 14144-14150.

(48) Rochet, A.; Baubet, B.; Moizan, V.; Devers, E.; Hugon, A.; Pichon, C.; Payen, E.; Briois, V.: Intermediate Species Revealed During Sulfidation of Bimetallic Hydrotreating Catalyst: A Multivariate Analysis of Combined Time-Resolved Spectroscopies. *J. Phys. Chem. C* **2017**, *121*, 18544-18556.

(49) Müller, A.; Weinstock, N.; Schmidt, K. H.; Nakamoto, K.; Schläpfer, C. W.: Raman-Spektren Von $(NH_4)2MoO_2S_2$ Mit ^{92}Mo Und ^{100}Mo. *Spectrochim. Acta, Part A: Molecular Spectroscopy* **1972**, *28*, 2289-2293.

(50) Junquera, J.; Cohen, M. H.; Rabe, K. M.: Nanoscale Smoothing and the Analysis of Interfacial Charge and Dipolar Densities. *J. Phys.: Condens. Matter* **2007**, *19*, 213203.

(51) Even, J.; Pedesseau, L.; Kepenekian, M.: Electronic Surface States and Dielectric Self-Energy Profiles in Colloidal Nanoscale Platelets of Cdse. *Phys. Chem. Chem. Phys.* **2014**, *16*, 25182-25190.

(52) Sapori, D.; Kepenekian, M.; Pedesseau, L.; Katan, C.; Even, J.: Quantum Confinement and Dielectric Profiles of Colloidal Nanoplatelets of Halide Inorganic and Hybrid Organic–Inorganic Perovskites. *Nanoscale* **2016**, *8*, 6369-6378.

(53) Shi, N.; Ramprasad, R.: Atomic-Scale Dielectric Permittivity Profiles in Slabs and Multilayers. *Phys. Rev. B* **2006**, *74*, 045318.

(54) Shi, N.; Ramprasad, R.: Dielectric Properties of Ultrathin SiO_2 Slabs. *Appl. Phys. Lett.* **2005**, *87*, 262102.

Conflicts of interest

The authors declare no competing interests.

TOC Graphic